

Tensor Asymmetry A_{zz} in the $x > 1$ Region

A Proposal to Jefferson Lab PAC 42

E. Long,^{† ‡} K. Slifer,[†] P. Solvignon[†]

University of New Hampshire, Durham, NH 03861

D. Day,[†] D. Keller[†]

University of Virginia, Charlottesville, VA 22903

D. Higinbotham[†]

Thomas Jefferson National Accelerator Facility, Newport News, VA 23606

M. Strikman

Pennsylvania State University, University Park, PA 16802

[†]Spokesperson

[‡]Contact: ellie@jlab.org

Abstract

The tensor-polarized target asymmetry, A_{zz} , which is used to extract b_1 in the DIS region through the $D(e, e')X$ channel, can be used to extract information on nucleon-nucleon interactions in the quasi-elastic region. The reaction is unique in that it can probe color transparency, which has never been explored at Jefferson Lab, and improve understanding of the deuteron wave function and particularly probe how short range correlations arise from proton-neutron interactions.

In the quasi-elastic region, A_{zz} was first calculated in 1988 by Frankfurt and Strikman, using the Hamada-Johnstone and Reid soft-core wave functions [1]. Recent calculations by M. Sargsian revisit A_{zz} in the $x > 1$ range using virtual-nucleon and light-cone methods, which differ by up to a factor of two [2].

An experimental determination of A_{zz} could be performed utilizing equipment identical for E13-12-011 at five different Q^2 values over the course of 24 days, with [NUMBER] additional days of commissioning. The measurements are less sensitive to the target polarization than E13-12-011, such that this experiment could be used to prove that the condition of 30% in-beam polarization is met for E13-12-011.

Contents

| | | |
|----------|---|----------|
| 1 | Background and Motivation | 4 |
| 1.1 | Probing the Deuteron Wavefunction | 4 |
| 2 | The Proposed Experiment | 6 |
| 2.1 | Experimental Method | 6 |
| 2.1.1 | Statistical Uncertainty | 8 |
| 2.1.2 | Systematic Uncertainty | 8 |
| 2.2 | Kinematics | 10 |
| 2.3 | Overhead | 14 |
| 2.4 | Polarized Target | 14 |
| 2.4.1 | Polarization Analysis | 16 |
| 2.4.2 | Tensor Polarization Enhancement | 17 |
| 2.4.3 | Depolarizing the Target | 17 |
| 2.4.4 | Rendering Dilution Factor | 19 |

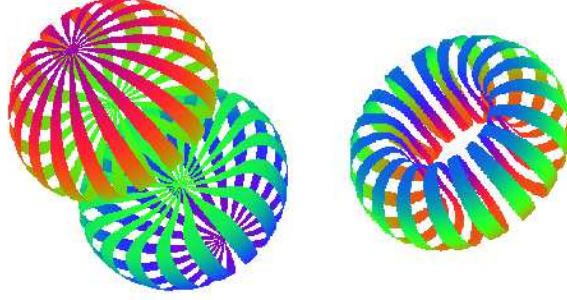


Figure 1: Equidensity lines of the deuteron in its two spin projections, $M_J = \pm 1$ and $M_J = 0$, respectively. Reproduced from [5, 3].

1 Background and Motivation

The deuteron is the simplest composite nuclear system, and in many ways it is as important to understanding bound states in QCD as the hydrogen atom was to understanding bound systems in QED. Our experimental and theoretical understanding of the deuteron remains unsatisfying. By taking a ratio of cross sections from electron scattering off of tensor-polarized and unpolarized deuterons, the S- and D-wave states can be disentangled, leading to a fuller understanding of the repulsive nucleon core.

Due to their small size and simple structure, tensor polarized deuterons are ideal for studying nucleon-nucleon interactions. Tensor polarization enhances the D-state wavefunction, which compresses the deuteron to ~ 0.5 fm [3] in a toroid as shown in Fig. 1, and has been noted to be revealing of short-range QCD effects. Understanding the nucleon-nucleon potential of the deuteron is essential for understanding short-range correlations [4]. To resolve the short-range structure of nuclei on the level of nucleon and hadronic constituents, we need processes that transfer to the nucleon constituents both energy and momentum larger than the scale of the NN short-range correlations. By scanning over a large range of Q^2 , we can measure how these processes begin to dominate the tensor asymmetry A_{zz} .

Additionally, measuring A_{zz} in the quasi-elastic region will fill a gap in measurements done on tensor polarized deuterium. It is same observable used in the elastic region to measure T_{20} , by $A_{zz} \propto T_{20}$. In the deep inelastic region, A_{zz} will soon be measured to extract the tensor structure function b_1 by the relation $A_{zz} \propto \frac{b_1}{F_1^D}$. Not only will measuring A_{zz} in the quasi-elastic region provide information necessary for understanding the wavefunctions of the deuteron, but it will bridge a hole in measurements of electron scattering from tensor-polarized deuterons.

1.1 Probing the Deuteron Wavefunction

It was suggested for some time [6] that to resolve the microscopic structure of nuclei one needs to study scattering at sufficiently large momentum transfer and large relative momenta of the produced nucleons. Effectiveness of this logic was confirmed [4] by a series of the experiments at SLAC [7] and JLab [8, 9] which directly observed short-range correlations (SRC) in a series of nu-

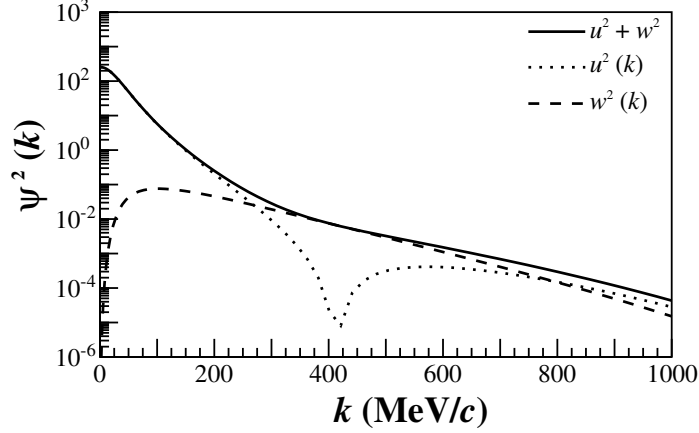


Figure 2: The AV18 [11] deuteron wave-function, showing the dominance of the D-state (w) at high momentum ($k > 300$ MeV/c).

clei and established similarity of the SRC in the deuteron and heavier nuclei with pn correlations giving dominant contribution. Hence, the deuteron serves as a “hydrogen atom” for the studies of the microscopic short-range structure of the nuclei.

Thus to achieve further progress of the field, it is necessary to improve our knowledge of the deuteron wave function at high momenta and especially to separate the contributions to the high momentum component of the deuteron, the S- and D-waves. Note here that the dominance of the D-wave at large range of the nucleon momenta is expected in a range of the theoretical models as shown in Fig. 2, but experimentally it was probed in a rather indirect way via measurement of T_{20} for the deuteron form factor [10]. Still the knowledge of S/D ratio for large momenta is rather poor. Indeed, all wavefunctions are constrained by low energy data to reproduce S/D ratio at small momenta while the overall probability of the D-wave in the deuteron differs by a factor up to 1.5, leading to a large difference of the S/D ratio at large momenta.

The experience with the studies of the ratios of the (e, e) cross sections at $x > 1$ has demonstrated an early onset of the scaling of the ratios when plotted as a function of the light-cone fraction of the struck nucleon momentum. As a result, the ratios were providing a direct measure of the ratio of the high momentum components in nuclei. Similarly, one can expect that in the case of scattering of the polarized deuteron we expect the early scaling for the asymmetry when plotted as a function of the minimal struck nucleon momentum or the light cone fraction in the $A(e, e)$ case. It was observed at JLab that the scaling of the ratios is setting in starting at $Q^2 \sim 1 \text{ GeV}^2$ so covering the range of Q^2 up to 2 GeV^2 should be sufficient to measure the S/D ratios in an interesting momentum range. The S- and D-states are related to the tensor asymmetry A_{zz} by [1]

$$A_{zz} \propto \frac{\frac{1}{2}w^2(k) - u(k)w(k)\sqrt{2}}{u^2(k) + w^2(k)}, \quad (1)$$

where $u(k)$ is the S-state wave function and $w(k)$ is the D-state wave function. Additionally, measuring A_{zz} at lower Q^2 will map out the transition from hadronic to partonic degrees of freedom.

It is worth noting here that on the top of comparing predictions for the different wave functions, one expects to be able to distinguish between non-relativistic and light cone quantum mechanic models. The principal difference between the models is the relation between the spectator momentum and momentum in the wave function - in the nonrelativistic model they coincide, while in the light cone model the relation is non-linear starting at $k \sim 250 \text{ MeV}/c$. This difference is most clearly manifested in the scattering off the polarized deuteron due to a strong dependence of the S/D ratio on the nucleon momentum.

2 The Proposed Experiment

2.1 Experimental Method

As in the case for E12-13-011, the measured double differential cross section for a spin-1 target characterized by a vector polarization P_z and tensor polarization P_{zz} is expressed as,

$$\frac{d^2\sigma_p}{d\Omega dE'} = \frac{d^2\sigma_u}{d\Omega dE'} \left(1 - P_z P_B A_1 + \frac{1}{2} P_{zz} A_{zz} \right), \quad (2)$$

where, σ_p (σ_u) is the polarized (unpolarized) cross section, P_B is the incident electron beam polarization, and A_1 (A_{zz}) is the vector (tensor) asymmetry of the virtual-photon deuteron cross section. This allows us to write the polarized tensor asymmetry with $0 < P_{zz} \leq 1$ using an unpolarized electron beam as

$$A_{zz} = \frac{2}{P_{zz}} \left(\frac{\sigma_p - \sigma_u}{\sigma_u} \right). \quad (3)$$

The tensor polarization is given by

$$P_{zz} = \frac{n_+ - 2n_0 + n_-}{n_+ + n_- + n_0}, \quad (4)$$

where n_m represents the population in the $m_z = +1, -1$, or 0 state.

Eq. 3 reveals that the asymmetry A_{zz} compares two different cross sections measured under different polarization conditions of the target: positively tensor polarized and unpolarized. To obtain the relative cross section measurement in the same configuration, the same target cup and material will be used at alternating polarization states (polarized vs. unpolarized), and the magnetic field providing the quantization axis will be oriented along the beamline at all times. This field will always be held at the same value, regardless of the target material polarization state. This process, identical to that used for the E12-13-011 b_1 measurement, ensures that the acceptance remains consistent within the stability (10^{-4}) of the super conducting magnet.

Since many of the factors involved in the cross sections cancel in the ratio, Eq. 3 can be expressed in terms of the charge normalized, efficiency corrected numbers of tensor polarized (N_p) and unpolarized (N_u) counts,

$$A_{zz} = \frac{2}{f P_{zz}} \left(\frac{N_p - N_u}{N_u} \right). \quad (5)$$

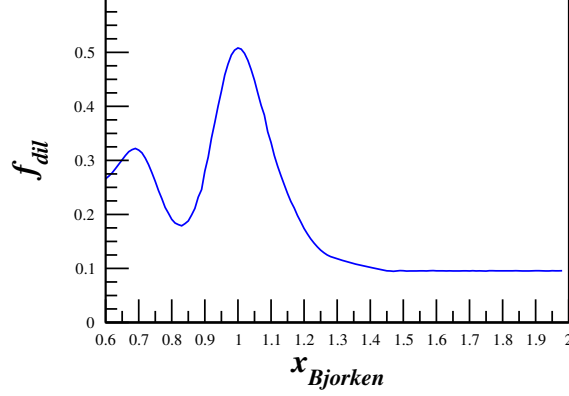


Figure 3: The estimated dilution factor, in this case at $Q^2 = 1.5 \text{ (GeV/c)}^2$, is expected to drop off at high x until it reaches the SRC plateau region. This effect will be counteracted by using a high-luminosity solid target.

The dilution factor f corrects for the presence of unpolarized nuclei in the target and is defined by

$$f = \frac{N_D \sigma_D}{N_N \sigma_N + N_D \sigma_D + \sum_A N_A \sigma_A}, \quad (6)$$

where N_D is the number of deuterium nuclei in the target and σ_D is the corresponding inclusive double differential scattering cross section, N_N is the nitrogen number of scattered nuclei with cross section σ_N , and N_A is the number of other scattering nuclei of mass number A with cross section σ_A . As has been noted in previous work [1], the dilution factor at high x drops off considerably until the SRC plateau region, as shown in Fig. 3. By using a high-luminosity solid target and a low scattering angle $\theta_{e'}$, this effect will be counteracted.

The dilution factor can be written in terms of the relative volume ratio of ND_3 to LHe in the target cell, otherwise known as the packing fraction p_f . In our case of a cylindrical target cell oriented along the magnetic field, the packing fraction is exactly equivalent to the percentage of the cell length filled with ND_3 .

If the time is evenly split between scattering off of polarized and unpolarized ND_3 , the time necessary to achieve the desired precision δA is:

$$T = \frac{N_p}{R_p} + \frac{N_u}{R_u} = \frac{8}{f^2 P_{zz}^2} \left(\frac{R_p(R_u + R_p)}{R_u^3} \right) \frac{1}{\delta A_{zz}^2} \quad (7)$$

where $R_{p(u)}$ is the polarized (unpolarized) rate and $N_{p(u)}$ is the total estimated number of polarized (unpolarized) counts to achieve the uncertainty δA_{zz} .

| Source | Systematic |
|------------------------------------|------------|
| Polarimetry | 12% |
| Dilution/Packing fraction | 6.5% |
| Trigger/Tracking efficiency | 1.0% |
| Acceptance | 0.5% |
| Charge Determination | 1.0% |
| Detector resolution and efficiency | 1.0% |
| Total | 14% |

Table 1: Estimates of the scale dependent contributions to the systematic error of A_{zz} .

2.1.1 Statistical Uncertainty

To investigate the statistical uncertainty we start with the equation for A_{zz} using measured counts for polarized data (N_p) and unpolarized data (N_u),

$$A_{zz} = \frac{2}{fP_{zz}} \left(\frac{N_p}{N_u} - 1 \right). \quad (8)$$

The statistical error with respect to counts is then

$$\delta A_{zz} = \frac{2}{fP_{zz}} \sqrt{\left(\frac{\delta N_p}{N_u} \right)^2 + \left(\frac{N_p \delta N_u}{N_u^2} \right)^2}. \quad (9)$$

For $\delta N_{p(u)} = \sqrt{N_{p(u)}}$, the uncertainty becomes

$$\delta A_{zz} = \frac{2}{fP_{zz}} \sqrt{\frac{N_p(N_u + N_p)}{N_u^3}}, \quad (10)$$

which can't be simplified further due to the large expected asymmetry.

2.1.2 Systematic Uncertainty

Table 1 shows a list of the scale dependent uncertainties contributing to the systematic error in A_{zz} . With careful uncertainty minimization in polarization the relative error in P can be less than or equal to 3.9%, as demonstrated in the recent E08-027/E08-007 experiment [12] and nearly as good for the deuteron using multiple techniques to measure the NMR signal as discussed in [13]. With the use of a positive tensor enhanced target it has been projected to be able to achieve a relative error in P_{zz} better than 12% [13]. The uncertainty from the dilution in the polarized target is estimated to be about 6% over the range of kinematics points of interest. We consider separately the uncertainty in the packing fraction of the ammonia target contributes at a level of less than 3%.

Charge calibration and detector efficiencies are expected to be known better to 1%, but the impact of time-dependent drifts in these quantities must be carefully controlled.

Time dependent factors

Eq. 5 involves the ratio of counts, which leads to cancellation of several first order systematic effects. However, the fact that the two data sets will not be taken simultaneously leads to a sensitivity to time dependent variations which will need to be carefully monitored and suppressed. To investigate the systematic differences in the time dependent components of the integrated counts, we need to consider the effects from calibration, efficiency, acceptance, and luminosity between the two polarization states.

Fluctuations in luminosity due to target density variation can easily be kept to a minimum by keeping the material beads at the same temperature for both polarization states by control of the microwave and the LHe evaporation. The He vapor pressure reading can give accuracy of material temperature changes at the level of $\sim 0.1\%$. Beam rastering can also be controlled to a high degree.

The beam charge asymmetries between two helicity states using the luminosity monitors for experiment E06-010 has been shown to be at the level of 4×10^{-5} with a width of 2×10^{-4} . An additional estimate on the change in the BCM calibration constant is seen in experiment E08-027 resulting in a absolute deviation of 2×10^{-4} over the course of six days. We expect to be able to minimize long term drifts by careful thermal isolation of the BCMs, however resulting trends will be studied and corrections implemented.

The acceptance of each cup can only change as a function of time if the magnetic field changes. The capacity to set, reset, and hold the target superconducting magnet to a desired holding field causes a field uncertainty of only $\delta B/B = 0.01\%$. This implies that, like the cup length l , the acceptance \mathcal{A} for each polarization state is the same.

In order to look at the effect on A_{zz} due to drifts in beam current monitor calibration and detector efficiency, we rewrite Eq. 5 explicitly in terms of the raw measured counts N_p^c and N_u^c ,

$$\begin{aligned} A_{zz} &= \frac{2}{fP_{zz}} \left(\frac{N_p^c}{N_u^c} - 1 \right) \\ &= \frac{2}{fP_{zz}} \left(\frac{Q\varepsilon l\mathcal{A}}{Q_1\varepsilon_1 l\mathcal{A}} \frac{N_p}{N_u} - 1 \right) \end{aligned} \quad (11)$$

where Q represents the accumulated charge, and ε is the detector efficiency. The target length l and acceptance \mathcal{A} are identical in both states to first order.

We can then express Q_1 as the change in beam current measurement calibration that occurs in the time it takes to collect data in one polarization state before switching to another, such that $Q_1 = Q(1 - dQ)$. In this notation dQ is a dimensionless ratio of changes in different polarization states. A similar representation is used for drifts in detector efficiency leading to,

$$A_{zz} = \frac{2}{fP_{zz}} \left(\frac{N_p Q (1 - dQ) \varepsilon (1 - d\varepsilon)}{N_u Q \varepsilon} - 1 \right). \quad (12)$$

which simplifies to,

$$A_{zz} = \frac{2}{fP_{zz}} \left(\frac{N_p}{N_u} (1 - dQ - d\varepsilon + dQd\varepsilon) - 1 \right). \quad (13)$$

For estimates of the dQ and $d\varepsilon$ we turn to previous experimental studies. For HRS detector drift during the JLab transversity experiment E06-010, the detector response was measured such that the normalized yield for same condition over a three month period indicated little change ($< 1\%$). These measurement were then used to show that for short time (20 minutes periods between target spin flip), the detector drift was estimated to be less than 1% times the ratio of the time period between target spin flip and three months. For the present experiment we use the same estimate except for the period between target polarization states used is ~ 12 hours leading to an overall drift $d\varepsilon \sim 0.01\%$. A similar approach is used to establish an estimate for dQ using studies from the data from the E08-027 experiment resulting in $d\varepsilon \sim 0.01\%$.

To express A_{zz} in terms of the estimated experimental drifts in efficiency and current measurement we can write,

$$A_{zz} = \frac{2}{fP_{zz}} \left(\frac{N_1}{N} - 1 \right) \pm \frac{2}{fP_{zz}} d\xi. \quad (14)$$

This leads to a contribution to A_{zz} on the order of 1×10^{-3} ,

$$dA_{zz}^{drift} = \pm \frac{2}{fP_{zz}} d\xi = \pm 3.7 \times 10^{-3}. \quad (15)$$

For this estimate we assume only two polarization state changes in a day. If it is possible to increase this rate then the systematic effect in A_{zz} will decrease accordingly.

Naturally detector efficiency can drift for a variety of reasons, for example including fluctuations in gas quality, HV drift or drifts in the spectrometers magnetic field. All of these types of variation as can be realized both during the experiment though monitoring as well as systematic studies of the data collected. Checks on the consistency of the cross section data that can be use ensuring the quality of each run will be used in the asymmetry analysis. Regression can be use to correct for any long term drifts that are of a non-stochastic nature. Each of these systematic effects can mitigate the systematic uncertainty to ~ 0.001 . In the kinematic region proposed here, A_{zz} is expected to be large, on the order of 0.1 to 1.0, making any absolute errors on this scale only critical as the data and models pass through the x-axis. While typical false asymmetries in Hall C of 0.01 are acceptable for this proposed measurement, we are interested in a strict control of the systematics for further reduction.

2.2 Kinematics

We will measure the tensor asymmetry A_{zz} for $0.80 < x < 1.75$, $1.0 (\text{GeV}/c)^2 < Q^2 < 1.9 (\text{GeV}/c)^2$, and $0.59 < W < 1.09 \text{ GeV}$. Fig. 4 shows the planned kinematic coverage utilizing the Hall C HMS and SHMS spectrometers at forward angle.

The polarized ND_3 target is discussed in section 2.4. The magnetic field of the target will be held constant along the beamline at all times, while the target state is alternated between a polarized and unpolarized state. The tensor polarization and packing fraction used in the rates estimate are 30% and 0.65, respectively. The dilution fraction changes with x in the range of this measurement as shown in Fig. 5. With an incident electron beam current of 100 nA, the expected deuteron luminosity is $1.3 \times 10^{35} \text{ cm}^{-2}\text{s}^{-1}$.

| | E_0 (GeV) | Q^2 (GeV ²) | W (GeV) | E' (GeV) | $\theta_{e'}$ (deg.) | Rates (kHz) | PAC Time (hours) |
|------|----------------|------------------------------|--------------|---------------|-------------------------|----------------|---------------------|
| SHMS | 8.8 | 1.5 | 0.46 | 8.36 | 8.2 | 0.55 | 600 |
| SHMS | 6.6 | 0.7 | 0.60 | 6.50 | 8.2 | 4.08 | 90 |
| SHMS | 2.2 | 0.3 | 0.87 | 2.11 | 14.4 | 3.73 | 30 |
| HMS | 2.2 | 0.3 | 0.86 | 2.11 | 14.9 | 4.65 | 30 |

Table 2: Summary of the central kinematics and physics rates using the Hall C spectrometers.

| x | $Q^2 = 1.5 \text{ (GeV}/c)^2$ | | | $Q^2 = 0.7 \text{ (GeV}/c)^2$ | | | $Q^2 = 0.3 \text{ (GeV}/c)^2$ | | |
|------|-------------------------------|--|---|-------------------------------|--|---|-------------------------------|--|---|
| | f_{dil} | δA_{zz}^{stat} $\times 10^{-2}$ | δA_{zz}^{sys} $\times 10^{-2}$ | f_{dil} | δA_{zz}^{stat} $\times 10^{-2}$ | δA_{zz}^{sys} $\times 10^{-2}$ | f_{dil} | δA_{zz}^{stat} $\times 10^{-2}$ | δA_{zz}^{sys} $\times 10^{-2}$ |
| 0.80 | 0.205 | 0.55 | 0.74 | 0.175 | 0.67 | 0.74 | 0.298 | 0.44 | 0.74 |
| 0.90 | 0.274 | 0.41 | 1.68 | 0.375 | 0.29 | 1.68 | 0.462 | 0.27 | 1.68 |
| 1.00 | 0.507 | 0.22 | 0.03 | 0.518 | 0.21 | 0.02 | 0.521 | 0.26 | 0.02 |
| 1.10 | 0.333 | 0.45 | 2.46 | 0.409 | 0.33 | 1.99 | 0.431 | 0.38 | 1.63 |
| 1.20 | 0.174 | 1.21 | 4.91 | 0.264 | 0.70 | 3.98 | 0.301 | 0.70 | 3.25 |
| 1.30 | 0.120 | 2.49 | 7.37 | 0.174 | 1.35 | 5.98 | 0.193 | 1.27 | 4.88 |
| 1.40 | 0.108 | 3.87 | 9.82 | 0.156 | 2.34 | 7.97 | 0.144 | 2.05 | 6.50 |
| 1.50 | 0.096 | 6.23 | 12.3 | 0.133 | 3.14 | 9.96 | 0.100 | 3.42 | 8.13 |
| 1.60 | 0.096 | 8.50 | 14.0 | 0.110 | 5.21 | 12.0 | 0.086 | 4.38 | 9.75 |
| 1.70 | 0.095 | 11.5 | 14.0 | 0.096 | 7.48 | 13.9 | 0.063 | 6.76 | 11.4 |
| 1.80 | 0.096 | 14.7 | 14.0 | 0.096 | 9.79 | 14.0 | 0.056 | 8.28 | 13.0 |

Table 3: Summary of the expected statistical uncertainty after combining overlapping x-bins. Values represent the statistics weighted average of all events that satisfy our kinematic cuts.

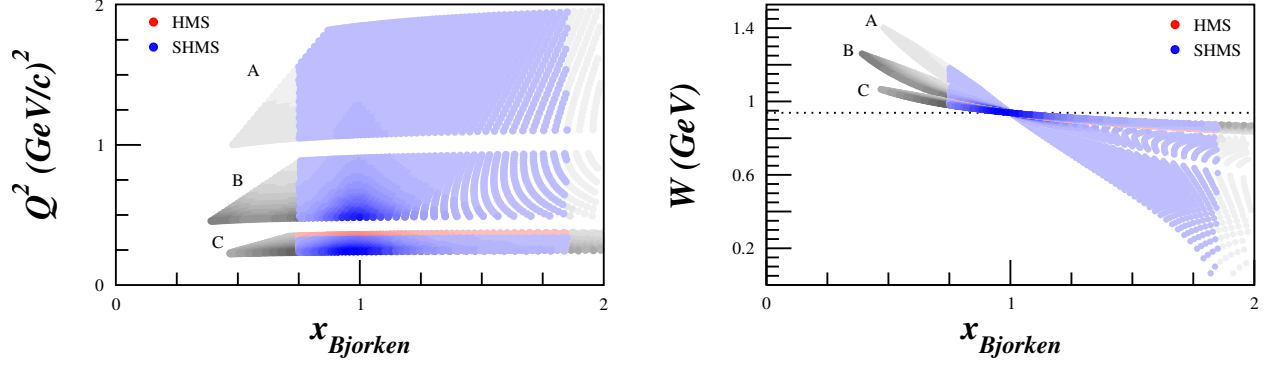


Figure 4: Kinematic coverage for central kinematic settings (not statistics weighted averaged) at $Q^2 = 1.5$ $(\text{GeV}/c)^2$ (A), 0.7 $(\text{GeV}/c)^2$ (B), and 0.3 $(\text{GeV}/c)^2$ (C). The grey regions are not included in our statistics estimates since they fall outside of $0.80 < x < 1.75$. Darker shading represents areas with higher statistics for each setting.

The momentum bite and the acceptance were assumed to be $\Delta P = \pm 8\%$ and $\Delta\Omega = 5.6$ msr for the HMS, and $\Delta P = {}^{+20\%}_{-8\%}$ and $\Delta\Omega = 4.4$ msr for the SHMS. For the choice of the kinematics, special attention was taken onto the angular and momentum limits of the spectrometers: for the HMS, $10.5^\circ \leq \theta \leq 85^\circ$ and $1 \leq P_0 \leq 7.3$ GeV/c, and for the SHMS, $5.5^\circ \leq \theta \leq 40^\circ$ and $2 \leq P_0 \leq 11$ GeV/c. In addition, the opening angle between the spectrometers is physically constrained to be larger than 17.5° . The dilution factors and projected uncertainties in A_{zz} are summarized in Table 3 and displayed in Fig. 6.

A total of 30 days of beam time is requested for production data, with an additional 8.6 days of expected overhead.

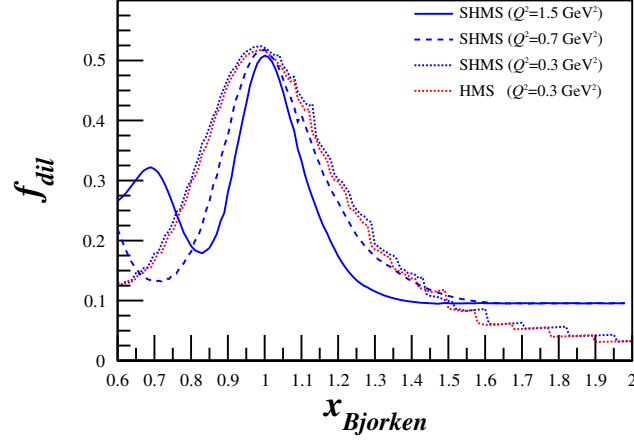


Figure 5: Projected dilution fraction covering the entire x range to be measured using a combination of P. Bosted's [14] and M. Sargsian's [15] code for the SHMS and HMS.

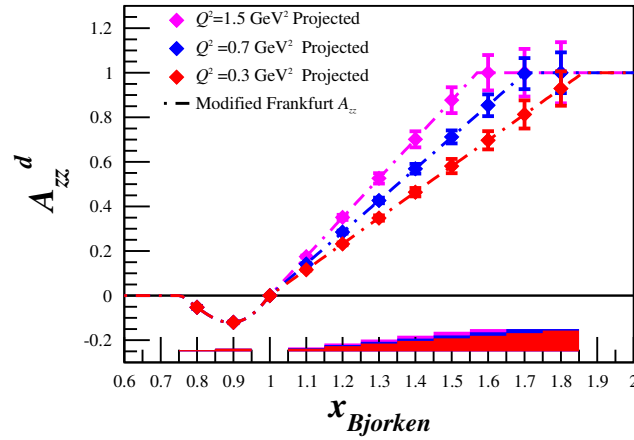


Figure 6: Projected statistical errors for the tensor asymmetry A_{zz} with 30 days of beam time. The band represents the systematic uncertainty. Also shown is the Frankfurt and Strikman model [1] that has been modified to estimate the plateau changing with Q^2 .

| Overhead | Number | Time Per (hr) | (hr) |
|--------------------------------|--------|---------------|----------|
| Polarization/depolarization | 35 | 2.0 | 70.0 |
| Target anneal | 13 | 4.0 | 52.0 |
| Target T.E. measurement | 5 | 4.0 | 20.0 |
| Target material change | 4 | 4.0 | 16.0 |
| Packing Fraction/Dilution runs | 6 | 1.0 | 6.0 |
| BCM calibration | 8 | 2.0 | 16.0 |
| Optics | 3 | 4.0 | 12.0 |
| Linac change | 1 | 8.0 | 8.0 |
| Momentum/angle change | 3 | 2.0 | 6.0 |
| | | | 8.6 days |

Table 4: Major contributions to the overhead.

2.3 Overhead

Table 4 summarizes the expected overhead, which sums to 8.6 days. The dominant overhead comes from switching from the polarized to unpolarized state and vice versa, and target anneals. The target will need to be annealed about every other day, and the material replaced once a week. Measurements of the dilution from the unpolarized materials contained in the target, and of the packing fraction due to the granular composition of the target material will be performed with a carbon target.

2.4 Polarized Target

This experiment will use the JLab/UVa dynamically polarized solid ND_3 target operated in longitudinal mode. The target is typically operated with a specialized slow raster and beamline instrumentation capable of characterizing the low current 50-100 nA beam. All of these requirements have been met previously in Hall C. The polarized target (see Fig. 7), has been successfully used in experiments E143, E155, and E155x at SLAC, and E93-026, E01-006 and E07-003, E08-027 and E08-007 at JLab. A similar target was used in Hall B for the EG1, EG4, and DVCS experiments.

The JLab/UVa target underwent significant renovation and improvement [16] during the recent g2p run. The magnet was replaced early in the run, and the target then performed consistently at or above historical levels. A new 1 K refrigerator and target insert were designed and constructed by the JLab target group. The cryogenic pumping system has been overhauled. In particular, the older Alcatel 2060H rotary vane pumps have been replaced with new Pfeiffer DU065 magnetically coupled rotary vane pumps, and the pump controls are being refurbished. The target motion system has been rebuilt from scratch.

The target operates on the principle of Dynamic Nuclear Polarization, to enhance the low temperature (1 K), high magnetic field (5 T) polarization of solid materials by microwave pumping. The polarized target assembly contains several target cells of 3.0 cm length that can be selected individually by remote control to be located in the uniform field region of a superconducting

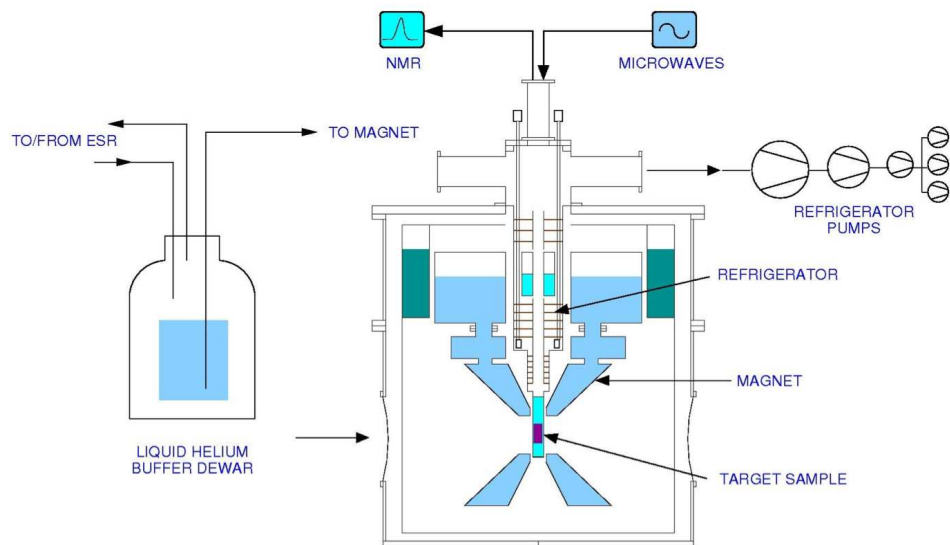


Figure 7: Cross section view of the JLab/UVa polarized target. Figure courtesy of C. Keith.

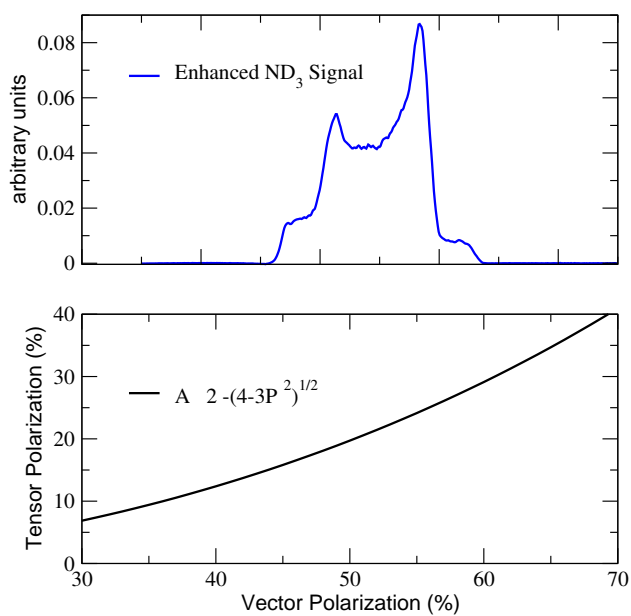


Figure 8: **Top:** NMR signal for ND_3 with a vector polarization of approximately 50% from the GEN experiment. **Bottom:** Relationship between vector and tensor polarization in equilibrium, and neglecting the small quadrupole interaction.

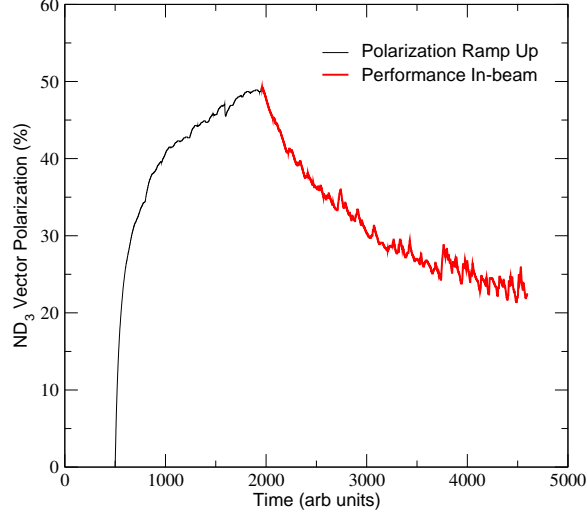


Figure 9: Performance of the ND₃ target during the GEN experiment.

Helmholtz pair. The permeable target cells are immersed in a vessel filled with liquid Helium and maintained at 1 K by use of a high power evaporation refrigerator. The coils have a 50° conical shaped aperture along the beam axis which allow for unobstructed forward scattering.

The target material is exposed to microwaves to drive the hyperfine transition which aligns the nucleon spins. The heating of the target by the beam causes a drop of a few percent in the polarization, and the polarization slowly decreases with time due to radiation damage. Most of the radiation damage can be repaired by periodically annealing the target, until the accumulated dose reached is greater than about $0.5 \times 10^{17} \text{ e}^-/\text{cm}^2$, at which time the target material needs to be replaced.

2.4.1 Polarization Analysis

The three Zeeman sublevels of the deuteron system ($m = -1, 0, 1$) are shifted unevenly due to the quadrupole interaction [17]. This shift depends on the angle between the magnetic field and the electrical field gradient, and gives rise to two separate transition energies. Hence, the unique double peaked response displayed in Fig. 8. When the system is at thermal equilibrium with the solid lattice, the deuteron polarization is known from:

$$P_z = \frac{4 + \tanh \frac{\mu B}{2kT}}{3 + \tanh^2 \frac{\mu B}{2kT}} \quad (16)$$

where μ is the magnetic moment, and k is Boltzmann's constant. The vector polarization can be determined by comparing the enhanced signal with that of the TE signal (which has known polarization). This polarimetry method is typically reliable to about 5% relative.

Similarly, the tensor polarization is given by:

$$P_{zz} = \frac{4 + \tanh^2 \frac{\mu B}{2kT}}{3 + \tanh^2 \frac{\mu B}{2kT}} \quad (17)$$

From Eqs. 16 and 17, we find:

$$P_{zz} = 2 - \sqrt{4 - 3P_z^2}$$

In addition to the TE method, polarizations can be determined by analyzing NMR lineshapes as described in [18] with a typical 7% relative uncertainty. At high polarizations, the intensities of the two transitions differ, and the NMR signal shows an asymmetry R in the value of the two peaks, as shown in Fig. 8. The vector polarization is then given by:

$$P_z = \frac{R^2 - 1}{R^2 + R + 1} \quad (18)$$

and the tensor polarization is given by:

$$P_{zz} = \frac{R^2 - 2R + 1}{R^2 + R + 1} \quad (19)$$

This measuring technique can be used as a compliment to the TE method resulting in reduced uncertainty in polarization.

2.4.2 Tensor Polarization Enhancement

It is possible to enhance tensor polarization using rf irradiation on the oriented deuterium nuclei to manipulate the alignment. Applying a saturating rf field on the pedestal of the smaller transition equalizes the substate $m = +1$ and $m = 0$ populations over 2/3 of the NMR signal. This equalization over the range of a single pedestal leads to enhancement in tensor polarization with only a small loss to the overall area ($\sim 2\%$). Recent studies at UVA using deuterated butanol have resulted in a tensor polarization of more than 25% as shown in Fig. 10. A similar result is expect for ND_3 . The studies also indicate that microwaves used during DNP does not interfere with the saturation from the rf irradiation when sufficient power is used. This implies that rf over the pedestal can be done the same time DNP is performed to enhance the area while taking beam in an experiment. Research and development is ongoing to study various techniques to optimize tensor enhancement for nuclear experiments targets.

2.4.3 Depolarizing the Target

To move from polarized to unpolarized measurements, the target polarization will be annihilated using destructive NMR loop field changes and destructive DNP microwave pumping. It is also possible to remove LHe in the nose of the target to remove the polarization by heating. During unpolarized data taking the incident electron beam heating is enough to remove the thermal equilibrium polarization.

The NMR measurement will ensure zero polarization. The target material will be kept at ~ 1 K for polarized and unpolarized data collection, and the target field will be held constant for both states as well. These consistencies are used to minimize the systematic differences in the polarized and unpolarized data collection. To minimize systematic effects over time, the polarization condition will be switched twice in a 72 hour period, as shown in Fig. 11. This is expected to account for drift in integrated charge accumulation.

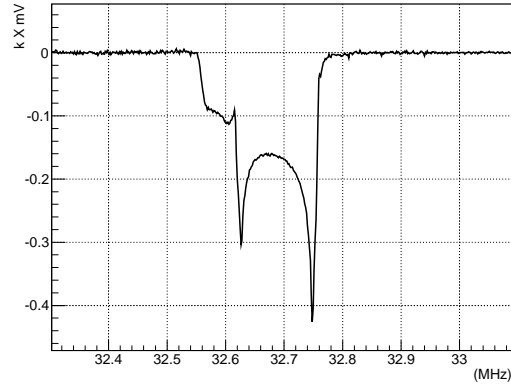


Figure 10: The deuterium magnetic resonance line shape showing tensor polarization of more than 25% after rf saturation of a pedestal.

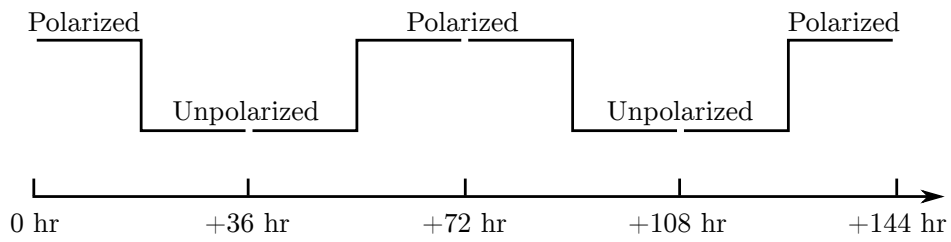


Figure 11: A visual demonstration of how the polarization cycle will happen over a 72 hour period to reduce time-dependent systematic effects. For the two lower Q^2 measurements, the cycle will happen over a 18 hour period.

2.4.4 Rendering Dilution Factor

To derive the dilution factor, we first start with the ratio of polarized to unpolarized counts. In each case, the number of counts that are actually measured, neglecting the small contributions of the thin aluminium cup window materials, NMR coils, etc., are

$$N_1 = Q_1 \varepsilon_1 \mathcal{A} l_1 [(\sigma_N + 3\sigma_1)p_f + \sigma_{He}(1 - p_f)], \quad (20)$$

and

$$N = Q \varepsilon \mathcal{A} l [(\sigma_N + 3\sigma)p_f + \sigma_{He}(1 - p_f)]. \quad (21)$$

where Q represents accumulated charge, ε is the dectector efficiency, \mathcal{A} the cup acceptance, and l the cup length.

For this calculation we assume similar charge accumulation such that $Q \simeq Q_1$, and that the efficiencies stay constant, in which case all factors drop out of the ratio leading to

$$\begin{aligned} \frac{N_1}{N} &= \frac{(\sigma_N + 3\sigma_1)p_f + \sigma_{He}(1 - p_f)}{(\sigma_N + 3\sigma)p_f + \sigma_{He}(1 - p_f)} \\ &= \frac{(\sigma_N + 3\sigma(1 + A_{zz}P_{zz}/2))p_f + \sigma_{He}(1 - p_f)}{(\sigma_N + 3\sigma)p_f + \sigma_{He}(1 - p_f)} \\ &= \frac{[(\sigma_N + 3\sigma)p_f + \sigma_{He}(1 - p_f)] + 3\sigma A_{zz}P_{zz}/2}{(\sigma_N + 3\sigma)p_f + \sigma_{He}(1 - p_f)} \\ &= 1 + \frac{3\sigma A_{zz}P_{zz}/2}{(\sigma_N + 3\sigma)p_f + \sigma_{He}(1 - p_f)} \\ &= 1 + \frac{1}{2}f A_{zz}P_{zz}, \end{aligned} \quad (22)$$

where $\sigma_1 = \sigma(1 + A_{zz}P_{zz}/2)$ has ben substituted, per Eq. 2, with $P_B = 0$. It can be seen that the above result corresponds to Eq. 5.

References

- [1] L. Frankfurt and M. Strikman, Phys.Rept. **160**, 235 (1988).
- [2] M. Sargsian, private communication, to be published.
- [3] J. L. Forest *et al.*, Phys. Rev. **C54**, 646 (1996).
- [4] J. Arrington, D. Higinbotham, G. Rosner, and M. Sargsian, Prog.Part.Nucl.Phys. **67**, 898 (2012).
- [5] J. Carlson and R. Schiavilla, Rev. Mod. Phys. **70**, 743 (1998).
- [6] L. L. Frankfurt and M. I. Strikman, Phys. Rept. **76**, 215 (1981).
- [7] L. Frankfurt, M. Strikman, D. Day, and M. Sargsian, Phys.Rev. **C48**, 2451 (1993).
- [8] J. Arrington, C. Armstrong, T. Averett, O. K. Baker, L. de Bever, *et al.*, Phys.Rev.Lett. **82**, 2056 (1999).
- [9] N. Fomin, J. Arrington, R. Asaturyan, F. Benmokhtar, W. Boeglin, *et al.*, Phys.Rev.Lett. **108**, 092502 (2012).
- [10] M. Garcon and J. Van Orden, Adv.Nucl.Phys. **26**, 293 (2001).
- [11] S. Veerasamy and W. N. Polyzou, Phys. Rev. C **84**, 034003 (2011).
- [12] D. Keller, Nucl. Inst. and Meth. **A728**, 133 (2013).
- [13] D. Keller, XVth International Workshop on Polarized Sources, Targets, and Polarimetry **PoS(PSTP2013)010**, (2013).
- [14] P. Bosted and V. Mamyan, (2012).
- [15] M. Sargsian, private communication.
- [16] C. Keith, JLab polarized target group. Private communication.
- [17] W. Meyer *et al.*, Nucl. Instrum. Meth. **A244**, 574 (1986).
- [18] C. Dulya *et al.*, Nucl. Instrum. Meth. **A398**, 109 (1997).